Applied Surface Science 625 (2023) 157207

Contents lists available at ScienceDirect

Applied Surface Science

journal homepage: www.elsevier.com/locate/apsusc

Full Length Article

Promotion of MgO sorbents with eutectic carbonate doping for high-temperature and pressure CO_2 capture

Hua Pang [a], Feng Mao [a], Shishun Zhang [a], Peng Sun [a], Anwei Sun [c], Gang Xiao [b,c,*]

[a] Guangdong Provincial Key Laboratory of Nuclear Power Safety, China Nuclear Power Technology Research Institute, Shangbu Zhong Road, Shenzhen 518000, China
[b] Laboratory of Clean Energy and Carbon Neutrality of Zhejiang Province, Zhejiang University, Hangzhou, Zhejiang 310027, China
[c] State Key Laboratory of Clean Energy Utilization, Zhejiang University, 38 Zheda Road, Hangzhou 310027, China

ARTICLE INFO

Keywords:
CO_2 sorption
MgO-based sorbent
Elevated operating condition
Cyclic stability
Density functional theory

ABSTRACT

MgO-based sorbents are promising candidates for CO_2 capture as they are widely available and feasible in thermodynamics, but the development of MgO-based sorbents operating at elevated temperature and pressure is still a challenging task due to sintering. Herein, we selected eutectic carbonates with high melting point as promoters for the application under elevated conditions. Among various eutectic carbonates, MgO with eutectic ternary LiNaK carbonate (ETC) doping exhibited the highest MgO conversion thanks to crystal defects based on the XRD analysis. The highest CO_2 capture capacity of 0.73 $g_{CO2}/g_{sorbent}$ was obtained with 20 wt% ETC at 400 °C and 2 MPa. With further elevation of operating parameters to 540 °C and 5 MPa, the sample still shows a stable MgO conversion of 0.69 after 30 cycles, where the material exhibits a porous structure that inhibits the sintering. The density function theory calculations reveal that the LiNaK doping lowers the formation energy of surface oxygen vacancy, providing possibility for the subsequent oxygen ion migration. The deep K incorporation is most effective to promote the oxygen ion diffusion with decreased oxygen ion migration energy barrier from 3.68 to 2.04 eV. This study can guide the design of high-performance CO_2 sorbents at wider application conditions.

1. Introduction

The continuous increase of anthropogenic CO_2 emission is aggravating climate changes [1–4], where carbon capture and storage (CCS) is regarded as an important and key technology to alleviate the greenhouse effect considering that fossil fuels will occupy a predominant position in short term [5,6]. Among various CCS technologies, pre-combustion capture in the integrated gasification combined cycle (IGCC) has received much attention, where CO_2 is separated prior to combustion process with high CO_2 concentration [7]. In this case, the CO_2 capture is performed at 350–550 °C with CO_2 concentration of 15–60 mol% in 2–7 MPa total pressure [1,8], which makes MgO theoretically appropriate from a thermodynamic perspective [9,10].

MgO is a promising medium temperature sorbent due to its wide availability, high theoretical capacity, and low regeneration energy [9–12], however, its practical application is limited by the slow sorption kinetic and poor thermal stability. Although remarkable improvements of reaction rate and adsorption capacity could be realized by adding molten eutectic salts [13–15], its CO_2 capture capacity decreases upon repeated sorption-regeneration cycles due to the agglomeration of the MgO grains at high regeneration temperature. For instance, Zhao et al. reported that the capacity of ($NaNO_3$-$NaNO_2$)-MgO decreased by approximately 57% after 5 cycles under severe conditions [16].

To improve the cyclic stability of eutectic salt-doped MgO, various strategies have been adopted, mainly including structure modification, inert stabilizer doping and alkali carbonates doping. Triviño et al. synthesized the eutectic mixtures (EM)-MgO fibers with the EM encapsulated in a hollow MgO shell. The protective shell of MgO prevented the structural change, improving the cyclic stability [17]. Hiremath et al. reported that compared with EM-MgO sorbent, further addition of TiO_2 enhanced the cyclic stability thanks to the greater resistance towards aggregation, but decreased the sorption capacity [18]. Jin et al. and Cui et al. found that further addition of $CaCO_3$ into alkali metal salt-MgO could improve the cyclic stability, where the formed plate-like structure acts as skeleton to prevent the particle agglomeration. Nevertheless, under the severe desorption condition of 500 °C, it still suffered from a decay in CO_2 uptake [19–21].

A more recent study on MgO-based sorbent for CO_2 capture at 1–3

* Corresponding author.
E-mail address: xiaogangtianmen@zju.edu.cn (G. Xiao).

https://doi.org/10.1016/j.apsusc.2023.157207
Received 26 January 2023; Received in revised form 26 March 2023; Accepted 4 April 2023
Available online 8 April 2023

MPa, 360–520 °C has demonstrated that KNO_3-Na_2CO_3-MgO exhibited high CO_2 capture capacity and good cycling stability at 480 °C, 2 MPa, but with the operating parameter increasing to 510 °C, 3 MPa, it decreased significantly due to the formed dense and non-porous surface [22]. On the other hand, the solid Na_2CO_3-doped MgO sorbent without nitrate dopant prepared by ball-milling method presented a stable MgO conversion thanks to its strong skeleton structure, but its CO_2 capture capacity remains to be improved [23]. Therefore, despite the fact that the molten nitrate dopant tends to cause sintering, it is necessary for MgO to obtain high CO_2 capture capacity since it plays an essential role in the mass transfer process, where it acts as the liquid reaction medium to promote oxygen ions and CO_2 diffusion [14,18,23]. From above results, the development of an appropriate MgO-based sorbent with high and stable CO_2 uptake for application at harsh sorption conditions is still an important and challenging task.

The unstable performance of EM-promoted MgO sorbent over multiple cycles may be related to the structural rearrangement of EM [17,24]. With the formation of clumped $MgCO_3$ particles, the bulk of EM will be segregated into small clusters, which were uniformly distributed on the surface of MgO after the decomposition of $MgCO_3$ [25]. The uniformly distributed small clusters with lower viscosity at high operating temperature tend to migrate on the MgO surface and improve the wetting of MgO particles, resulting in liquid-phase sintering [26,27], which means that the promoter with low melting point is prone to cause sintering under elevated temperature and pressure conditions. If other EM with high melting point, such as eutectic carbonates, are used as a promoter for MgO at harsh conditions, it may improve the cyclic stability under harsh conditions. Furthermore, in our previous study, we noticed that for KNO_3-Na_2CO_3-MgO sorbent, higher Na_2CO_3 content can alleviate the sintering at sorption condition of 540 °C, 5 MPa due to the increased surface area [22]. Therefore, eutectic carbonates are presumedly suitable dopant for MgO, which may improve the pore structure allowing the sorbent maintain a high and stable CO_2 capture capacity. The density functional theory (DFT) was used to investigate the reaction mechanism between MgO and CO_2. Recently, the mechanism of interaction of H_2O and CO_2 molecules with MgO was uncovered through the analysis of adsorption energies, charge transfer, electronic localization function, adsorption/dissociation energy barriers [28]. If eutectic carbonates do improve the reactivity of MgO, the promotion mechanism can be explored through the DFT calculation.

In this work, eutectic carbonates with high melting point compared to molten nitrates were selected as promoters for MgO for the application under harsh conditions. The sorbents were synthesized using ball-milling method. The MgO conversion and cyclic performance of eutectic ternary LiNaK carbonate (ETC), eutectic binary LiNa and LiK carbonates-promoted MgO sorbent were investigated. Eutectic binary NaK carbonate was not taken into account, as its melting point is up to 710 °C [29]. Furthermore, the effect of ETC doping amounts and sorption conditions on the MgO conversion and cyclic performance were performed. In addition, the density functional theory (DFT) calculations were conducted to investigate the effect of LiNaK surface doping and further cation subsurface doping on the oxygen vacancy formation, structural stability and oxygen ion diffusion.

1.1. Experimental apparatus

A schematic diagram of the testing unit is illustrated in Fig. 1. The high-pressure reactor is the core component, where the high temperature and pressure carbonation reaction was conducted. The reactor body was a custom-made nickel-based alloy tube with inner and outer diameters of 40 and 70 mm, respectively, which was placed in a three-temperature-zone furnace with a total electric heating section length of 600 mm. The pressure of the system was controlled with a back-pressure regulator and the furnace temperature was controlled by a PID controller. An Omega K-type thermocouple was fixed at the center position of the reactor through the flange to ensure that the container was located at the same position during each run. The thermocouple was connected to the data acquisition system and the measured container temperature was regarded as the reaction temperature. The reaction time was measured with a stopwatch. Annular coiled tube structures were adopted in the preheating furnace and high-pressure reactor to prolong the gas heating time, and the exposed pipeline between them was insulated with the electric tracing band.

Before CO_2 sorption performance tests, all samples were calcined at 500 °C for 3 h in an N_2 atmosphere to remove the possible sorption gas and avoid interference to experimental results. During the cyclic stability test, the carbonation was carried out in the high-pressure reactor, and the decarbonation was performed in the atmospheric pressure tubular reactor. During the carbonation process, firstly, the back-pressure regulator was adjusted to the desired pressure, and the preheating furnace and high-pressure reactor were heated to the predetermined temperature. When the stable temperature was achieved, about 0.4 g of solid sorbent was weighed. Then, the ball valve working as the inlet of the reactor was opened, through which the container was

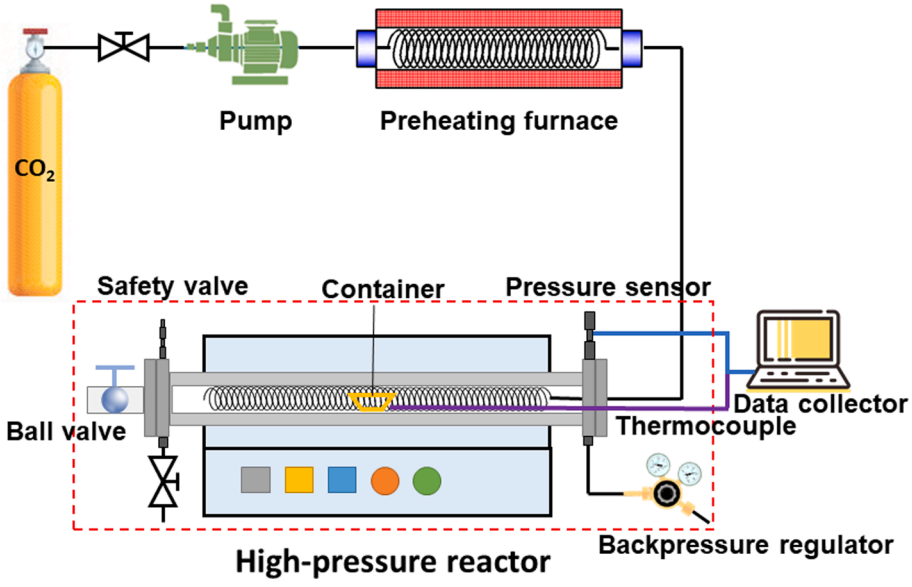

Fig. 1. Diagram of the high-pressure reactor.

pushed into the reactor until it contacted with the thermocouple at the center of the reactor. After that, the ball valve was closed, and the pressurized CO_2 gas charged into the reactor. After the reaction time was reached, the CO_2 gas was released. The sample was extracted rapidly through the opened ball valve and weighted with a delicate electronic balance. The MgO conversion and the CO_2 capture capacity were calculated as following equations:

$$\text{MgO conversion} = ((m - m_0)/(m_0 \times \omega_{MgO}))/(M_{CO_2}/M_{MgO}) \quad (1)$$

$$CO_2 \text{ capture capacity} = (m - m_0)/m_0,\ g_{CO_2}/g_{sorbent} \quad (2)$$

where m_0 is the initial sample weight, m is the sample weight after reaction, ω_{MgO} is the weight fraction of MgO in the sample, M_{MgO} and M_{CO2} represent the molar weights of MgO and CO_2.

2. Experimental and computational

2.1. Materials

Commercial magnesium oxide (MgO, GR) and lithium carbonate (Li_2CO_3, AR, ≥98.0%) are purchased from Shanghai Macklin Biochemical Co., Ltd. Sodium carbonate (Na_2CO_3, AR, ≥99.8%) and potassium carbonate (K_2CO_3, AR, ≥99.0%) are purchased from Sinopharm Chemical Reagent Co., Ltd. Eutectic LiNaK, LiK and LiNa carbonates are adopted as promoters for MgO, whose composition proportion and melting point are shown in Table 1.

2.2. Material preparation

For MgO-ETC, ETC composed of Li_2CO_3, Na_2CO_3 and K_2CO_3 with a melting point of 397 °C was firstly synthesized. The carbonates were weighted in the desired composition, then mechanically mixed in the vortex mixer (Kylin-Bell Lab Instruments, XM-80A) for 15 min, and finally the uniformly mixed salts were calcined in the air with temperature increasing from room temperature to 700 °C for 1 h and maintaining at 700 °C for 1 h in the muffle furnace to form a uniform distribution liquid mixture. After cooling, the solidified mixture was ground in the mortar until it visibly became fine.

After the synthesis of ETC, MgO-ETC was prepared using an SFM-3 ball mill (Hefei Kejing Materials Technology CO., LTD). 3.5 g of MgO and appropriate amounts of ETC were put into a plastic bottle (Nalgene, 50 mL). Then, the ball milling was carried out using 37 g of zirconia beads with rotation at a speed of 1200 rpm for 20 min. The zirconia beads consist of 16 g of beads with a diameter of 10 mm, 18 g of beads with a diameter of 8 mm and 3 g of beads with a diameter of 5 mm. LiNa-MgO and LiK-MgO sorbents were prepared following the same process as LiNaK-MgO sorbent.

2.3. Characterization

Phase compositions of all samples were analyzed via an X-ray diffractometer (XRD, PANalytical B.V. X-pert Power) using Cu-Kα radiation with a wavelength of 1.5406 Å, and it was operated at 40 KV and 40 mA. All samples were scanned within the 2θ range of 10-80° with a step size of 0.02°. The micromorphology of the samples was observed by a Scanning Electron Microscope (SEM, HITACHI SU-8010), and the element distribution of eutectic salts on the surface was measured with Energy Dispersive Spectroscopy (EDS) installed on SEM. The textual properties were evaluated from N_2 adsorption/desorption isotherms, which were obtained with a surface area and porosity analyzer (Micromeritics, ASAP2460).

Table 1
Composition of molten salt and the corresponding melting point.

Sample	Salt composition (wt.%)	Melting point (°C)
Li_2CO_3- Na_2CO_3-K_2CO_3	32.1–33.4–34.5	397 [30]
Li_2CO_3- K_2CO_3	46.59–53.41	483.9 [31]
Li_2CO_3- Na_2CO_3	42–58	498.3 [32]

2.4. Computational section

Based on the DFT method, all calculations were realized by using the Dmol3 module embedded in Material Studio software. The exchange–correlation energy was calculated via Generalized Gradient Approximation (GGA) formulated by Perdew-Burke-Ernzerhof (PBE) functional [33,34]. To describe the GGA functionals more appropriately, the semiempirical approach of Grimme was adopted to describe long-range electron correlations that are responsible for van der Waals force, which is crucial for the formation and stability of molecules and materials [35–37]. The all-electron wavefunction and double numerical basis set with polarization function (DNP) were selected [38]. For the slab calculation, the Monkhorst-Pack scheme was used in the Brillouin zone, and the k-point was set to 4 × 4 × 1. In the self-consistent field (SCF) calculation, the tolerance was set to 1×10^{-5}. The convergence criterion was set to 1×10^{-5} Ha for energy, 0.004 Ha/Å for maximum force and 0.005 Å for maximum displacement. The transition state (TS) of the oxygen migration process was obtained by linear synchronous transit/quadratic synchronous transit (LST/QST) method, and the obtained transition state structures were further identified by vibrational analysis.

The geometry of MgO was firstly optimized. The optimized lattice parameter of MgO was 4.209 Å, which was close to the experimental data (4.21 Å) [39]. Once the optimized unit cell of MgO was obtained, the most stable low-index MgO (1 0 0) surface was cleaved from the MgO unit cell, and the periodic supercell (2 × 2) with a vacuum thickness of 20 Å was constructed. The MgO (1 0 0) surface was considered in calculations, since this surface has the lowest surface energy, which is the most stable surface [40]. All calculations were conducted by keeping the atoms in the two bottom layers fixed. The oxygen vacancy formation energy, and migration barrier were defined as Eq. (3) and (4) [41,42]. Furthermore, the formation energy of the dopant on the surface and subsurface (the second layer) were compared to describe the difficulty of the doped structures, the formation energy formulas of which was described as Eq. (5)[43,44].

$$E_{Vo} = E_{defective} - E_{perfect} + 1/2E_{O_2} \quad (3)$$

$$E_a = E_{TS} - E_{IS} \quad (4)$$

$$E_{form} = \left(E_{LiNaK\text{ - }doped} + nE_{Mg}\right) - \left(E_{undoped} + xE_{Li} + yE_{Na} + zE_K\right) \quad (5)$$

where $E_{defective}$ and $E_{perfect}$ are the energy of the surface with and without an oxygen vacancy. E_{O_2} is the energy of an isolated O_2 molecule. It should be noticed that the O_2 are magnetic molecules with a triplet multiplicity, and the spin polarization should be considered in the calculation [45–47]. E_{TS} and E_{IS} represent the energy of the transition state and the initial structures. $E_{LiNaK\text{-}doped}$ and $E_{undoped}$ are the energy of the LiNaK doped and undoped structures of MgO surface with an oxygen vacancy after optimization. E_{Li}, E_{Na}, E_K and E_{Mg} are the energy of one atom of the bulk metal of Li, Na, K and Mg. n, x, y and z are the number of the replaced Mg and doped Li, Na and K.

3. Results and discussion

3.1. Characterization of synthesized sorbents

Fig. 2(a)-(c) show the SEM images and elemental maps of eutectic carbonates-doped MgO samples. From SEM images, all samples with various eutectic carbonate dopants were composed of aggregated particles. It was clearly observed that the (Li_2CO_3-Na_2CO_3)-doped MgO has a smaller particle size compared with Li_2CO_3-K_2CO_3 and ETC-doped

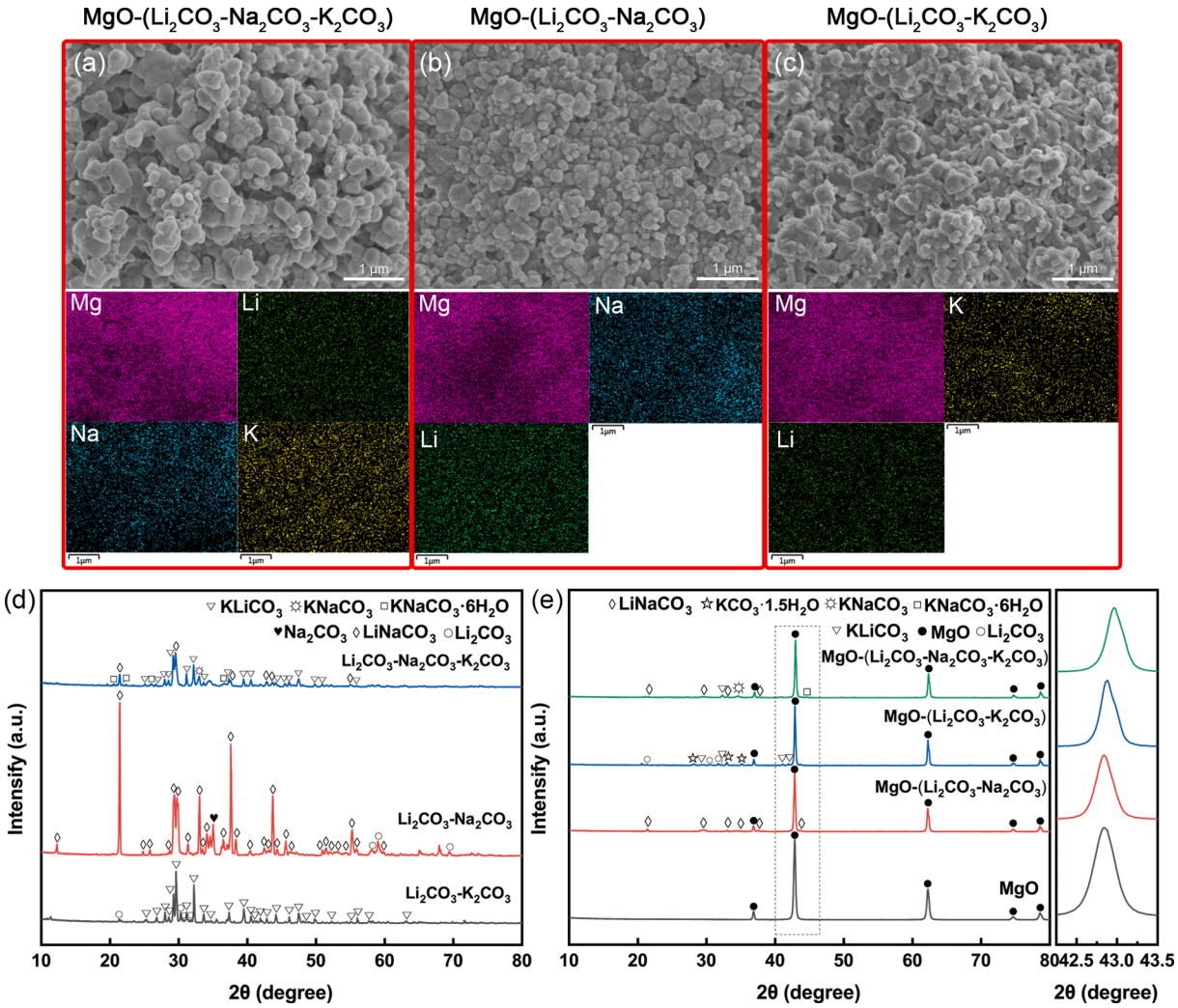

Fig. 2. SEM images and EDS elemental maps of (a) MgO-ETC, (b) MgO-(Li_2CO_3-Na_2CO_3) and (c) MgO-(Li_2CO_3-K_2CO_3). XRD patterns of (d) synthesized eutectic carbonates (ETC, Li_2CO_3-Na_2CO_3 and Li_2CO_3-K_2CO_3) and (e) eutectic carbonates-doped MgO samples (MgO, MgO-ETC, MgO-(Li_2CO_3-Na_2CO_3) and MgO-(Li_2CO_3-K_2CO_3)).

samples. After calculation by the image processing program (ImageJ), the average particle sizes of Li_2CO_3-Na_2CO_3, Li_2CO_3-K_2CO_3 and ETC-doped samples are corresponding to 152 nm, 194 nm and 208 nm, respectively, where the particle size increased with the decrease of melting points of eutectic carbonates, indicating that the eutectic salt with lower melting point is prone to cause particle aggregation. Furthermore, as observed from the SEM-EDS mapping of Fig. 2(a)-(c), no lumpy eutectic carbonates were observed, and all the elements were dispersed uniformly on the surface of the sorbent.

Fig. 2(d)-(e) show the XRD patterns of synthesized eutectic carbonates and the corresponding eutectic carbonate-doped MgO sorbents after preheating at 500 °C. The ETC was mainly composed of $LiNaCO_3$, $KLiCO_3$, $KNaCO_3$ and $KNaCO_3{\cdot}6H_2O$. As for Li_2CO_3-Na_2CO_3, many diffraction peaks indexed as $LiNaCO_3$ and few peaks assigned to Li_2CO_3 and Na_2CO_3 were detected, indicating that the reaction between Li_2CO_3 and Na_2CO_3 was not completed. For Li_2CO_3-K_2CO_3, many $KLiCO_3$ and several Li_2CO_3 peaks were found, and the unreacted Li_2CO_3 was due to the over-stoichiometric ratio of Li_2CO_3 to K_2CO_3. After doping into MgO, the MgO-ETC and MgO-(Li_2CO_3-Na_2CO_3) sorbents were mainly constituted by MgO and their corresponding double carbonate salts ($ABCO_3$, A and B = Li, Na, K), but for the MgO-(Li_2CO_3-K_2CO_3) sorbent, besides the double carbonate salt of $KLiCO_3$, Li_2CO_3 and $K_2CO_3{\cdot}1.5H_2O$ were detected, which was due to the uncompleted reaction between Li_2CO_3 and K_2CO_3 at 500 °C.

As shown in Fig. 2(e), it should be noted that the diffraction peak of the (200) face of eutectic carbonate-doped MgO samples shifted to higher angles compared with the pure MgO, which indicated that the cation of eutectic carbonates was incorporated into MgO and changed its lattice structure [19]. The shift angles gradually increased with the decreasing melting points of eutectic carbonate promoters, where the sample doped with the lowest melting point ETC exhibited the biggest angle shift, suggesting that the promoter with a low melting point was beneficial to the incorporation of cations into the crystal lattice of MgO.

3.2. *CO_2 sorption behavior of MgO-ETC sorbents*

The eutectic carbonates were selected as additives for MgO. The effects of eutectic carbonate species, ETC doping amounts and sorption conditions on the MgO conversion and cyclic performance were performed. During the cyclic test, the desorption process was carried out at 475 °C, 1 bar in pure N_2 for 25 min. The CO_2 uptake results for all figures have been added in the supplementary file.

Fig. 3(a) shows the effect of the amounts of ETC on the MgO conversion with sorption at 400 °C, 2 MPa. The highest MgO conversion of 0.38 was attained with 20 wt% ETC after 32 min of reaction with CO_2. All the samples exhibited a fast reaction rate in the early stage of the reaction, but after 2 min, the MgO conversion increased slowly with time. It seemed that the reaction entered the diffusion-controlled stage

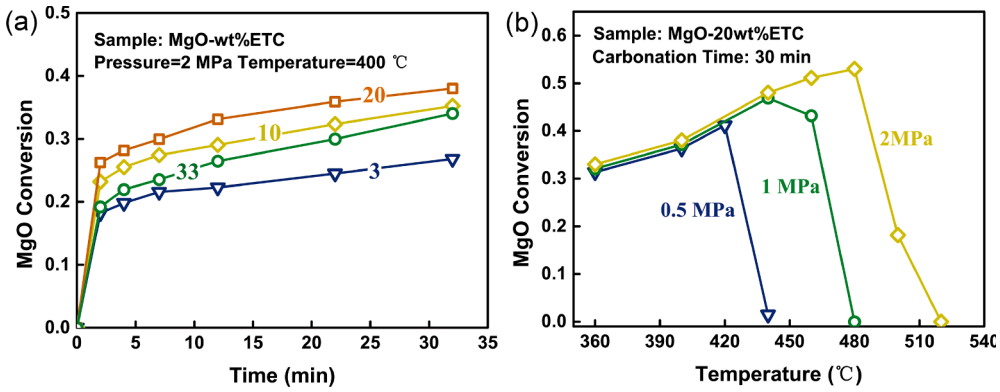

Fig. 3. (a) MgO conversion of MgO- wt%ETC with sorption at 400 °C, 2 MPa in pure CO_2 with different amounts of ETC, (b) the influence of sorption temperature on the MgO conversion at different pressure of CO_2.

after 2 min, which was attributed to the limited diffusion rate of oxygen ions and CO_2 during the sorption process. The temperature dependence of the MgO conversion after 30 mins of sorption in the pressure range 0.5–2 MPa is shown in Fig. 3(b), where the highest MgO conversion at 0.5, 1 and 2 MPa occurred at temperatures around 420, 440 and 480 °C, respectively. The difference in MgO conversion at low temperatures varied slightly with the pressure change, while at high temperatures it was significantly improved by the increase of pressure.

The cyclic stability of MgO doped with various eutectic carbonates, including ETC, Li_2CO_3-K_2CO_3 and Li_2CO_3-Na_2CO_3 was tested with sorption at the harsh condition of 515 °C, 5 MPa as shown in Fig. 4(a). Among all samples, MgO-ETC exhibited the best cyclic performance with the 1st and 30th MgO conversion of 0.6 and 0.93, respectively. The sample with Li_2CO_3-K_2CO_3 doping also presented a good cyclic stability with the 1st and 30th MgO conversion of 0.59 and 0.76, respectively. In comparison, MgO-(Na_2CO_3-K_2CO_3) presented the lowest MgO conversion, which decreased slightly from 0.47 to 0.42 after 30 cycles. The higher MgO conversion with ETC dopant may be related to the crystal defects of MgO as shown in Fig. 2(e), where more cations incorporated into the MgO crystal lattice and generated more crystal defects, improving the ions diffusion rate.

The cyclic stability of MgO doped with different amounts of ETC was examined with sorption at 400 °C, 2 MPa as shown in Fig. 4(b), where all the samples with ETC in the range of 10 wt%-33 wt% presented a significant increase in MgO conversion in the first several cycles. Moreover, the increase rate strongly depended on the content of the ETC. The

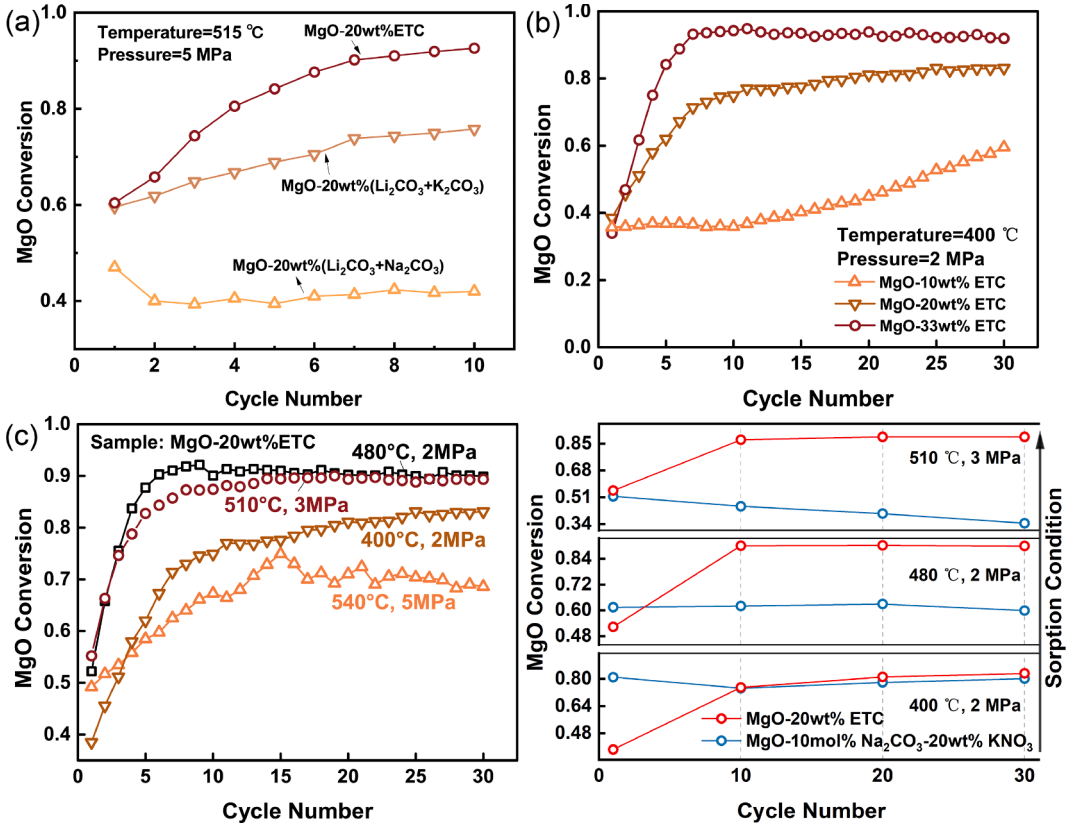

Fig. 4. (a) the cyclic test of samples with various eutectic carbonates (ETC, Li_2CO_3-K_2CO_3 and Li_2CO_3-Na_2CO_3) with sorption at 515 °C, 5 MPa in pure CO_2 for 20 min, (b) cyclic test of samples with different amounts of ETC with sorption at 400 °C, 2 MPa in pure CO_2 for 30 min, (c) cyclic test of MgO-20 wt%ETC under different sorption conditions with sorption for 30 min (at 540 °C, 5 MPa for 20 min), (d) improvement performance comparison of MgO-20 wt%ETC and MgO-10 mol% Na_2CO_3-20 wt%KNO_3 under different sorption conditions with sorption for 30 min.

sample with higher content of ETC (33 wt%) presented a fast increase rate, whose MgO conversion increased significantly from 0.34 to 0.93 in the first 7 cycles and then retained at almost 0.93 during the later cycles. In comparison, the sample with lower content of ETC (10 wt%) increased gradually from 0.36 to 0.59 during the 30 cycles. In addition, the corresponding CO_2 capture capacity of the sample with different amounts of ETC was shown in Fig. S2 (b), where the highest CO_2 capture capacity of 0.73 $g_{CO2}/g_{sorbent}$ was obtained with 20 wt% ETC.

The cyclic stability of MgO-20 wt%ETC was further examined in the operating parameter range 400 °C, 2 MPa-540 °C, 5 MPa as shown in Fig. 4(c), where the sample exhibited a remarkable increase in the MgO conversion during the first several cycles and then maintained a stable or gradually increased MgO conversion during the later cycles. The sample with operation at 480 °C, 2 MPa had the best performance, whose MgO conversion increased significantly in the first 7 cycles and then maintained at almost 0.9 during the later cycles. With a further elevation of the operating parameter to 510 °C, 3 MPa, although slight decrease in MgO conversion was observed compared to the test conducted at 480 °C, 2 MPa, there was no degradation in MgO conversion during the cyclic test. Even under the harsh condition of 540 °C, 5 MPa, the sample maintained a stable MgO conversion of 0.69, indicating that MgO-ETC is suitable as CO_2 sorbents with the application under severe sorption conditions.

To compare the improved performance of molten nitrates and eutectic carbonates promoters, the MgO conversion of MgO-20 wt%ETC and MgO-10 mol%Na_2CO_3-20 wt%KNO_3 at the 1st, 10th, 20th and 30th cycles were compared with the increasing of the sorption condition from 400 °C, 2 MPa to 510 °C, 3 MPa as shown in Fig. 4(d). Under the mild condition of 400 °C, 2 MPa, both samples presented a good cyclic stability, where MgO with KNO_3 doping showed a high MgO conversion compared to MgO-ETC at the 1st cycle, but a close value after the 10th cycle. With the increasing of sorption condition to 480 °C, 2 MPa, the MgO conversion of MgO-ETC is about 1.5 times higher than MgO-Na_2CO_3-KNO_3. Under the harsh condition of 510 °C, 3 MPa, MgO-ETC exhibited a stable MgO conversion of 0.9 after 30 cycles, while the MgO conversion of MgO-Na_2CO_3-KNO_3 decreased to 0.34. Therefore, ETC is more suitable as promoter than molten nitrates with sorption under severe conditions.

3.3. XRD and microstructure analysis for MgO-ETC

Fig. 5(a) shows the XRD patterns of the MgO-20 wt%ETC before and after the cyclic test with sorption at 400 °C, 2 MPa. After the 1st carbonation, many peaks indexed as $MgCO_3$ appeared along with weak MgO peaks. After the 30th carbonation, the peak intensity of $MgCO_3$ increased strongly with remarkable decreased MgO peaks, and no other new product phase was detected, indicating that the rapid increase of MgO conversion during the cyclic test was attributed to the increased reactivity of MgO, leading to the rapid formation of $MgCO_3$.

To clarify the microstructural evolution at different sorption conditions, morphologies of the MgO-20 wt% ETC after 30 cycles with different sorption conditions (400 °C, 2 MPa; 480 °C, 2 MPa; 510 °C, 3 MPa and 540 °C, 5 MPa) were analyzed. It can be observed from Fig. 5(c) that the fresh sample was composed of aggregated particles, which sintered into a lump and formed aggregates with obvious penetrating holes after 30 cycles with sorption at 400 °C, 2 MPa as shown in Fig. 5

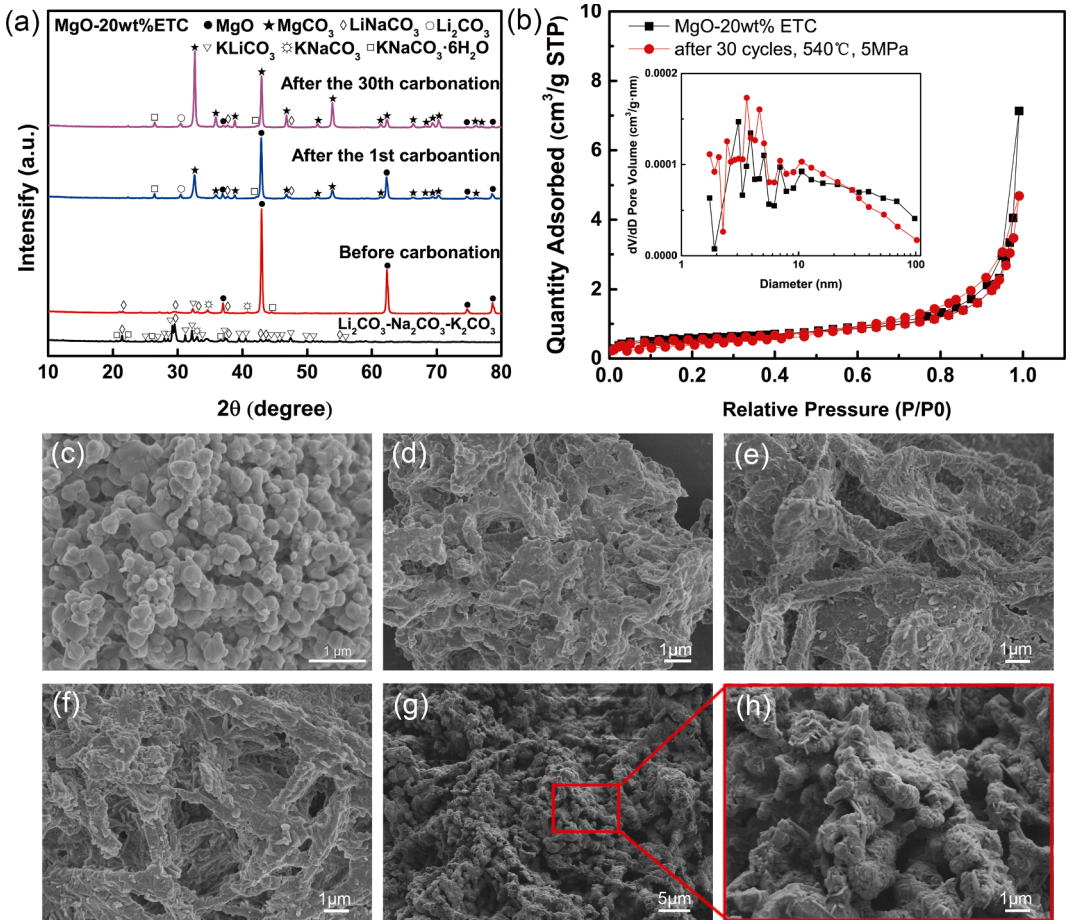

Fig. 5. (a) XRD patterns of the synthesized ETC, MgO-20 wt%ETC before and after the 1st and 30th carbonation in pure CO_2 at 400 °C, 2 MPa for 30 min, (b) N_2 adsorption–desorption isotherms and pore-diameter distribution (inset) of MgO-20 wt%ETC after the 30th desorption; morphology of MgO-20 wt%ETC with sorption at different conditions after 30 cycles, (c) fresh sample, (d) at 400 °C, 2 MPa, (e) at 480 °C, 2 MPa, (f) 510 °C, 3 MPa, and (g)-(h) 540 °C, 5 MPa.

(d). For the structures with sorption at 480 °C, 2 MPa and 510 °C, 3 MPa after 30 cycles, as shown in Fig. 5(e)-(f), the particles seemed to form interconnected skeletons. Benefited from the interconnected skeletons, it could remain a stable and a high MgO conversion after 30 cycles. Fig. 5 (g)-(h) exhibited the microstructure of the sample with sorption at 540 °C, 5 MPa after 30 cycles, where the phenomena of particle coarsening was obviously observed. The coarsening particles were coalesced and formed a structure with small pore channels. Despite the fact that the particle coarsening impedes the diffusion process of gas into the unreacted inner MgO, the sample maintained a stable MgO conversion of 0.69 at the harsh condition of 540 °C, 5 MPa thanks to the porous structure. The textural features of the sample before the reaction and after 30 cycles with sorption at 540 °C, 5 MPa were examined. The BET value slightly decreased from 1.99 m^2/g to 1.87 m^2/g after 30 cycles, and the pore-diameter distribution changed little as shown in the inset of Fig. 5 (b). The above results suggested that the ETC doping was an effective strategy to improve the cyclic stability under harsh conditions thanks to its good porous structure.

3.4. Computational analysis

In order to further explore the promotion mechanism of ETC doping on the MgO, DFT calculations were conducted to investigate the effect of cation incorporation on the oxygen vacancy formation, structural stability and oxygen ion diffusion. According to the related literature, the difficulty level of extra element doping mainly depends on the difference of ionic size and the charge imbalance between them. Despite the difference of the ionic size and the charge imbalance between alkali metal ions (Li, Na and K) and Mg, the evidence for the alkali metal ions (Li, Na and K) doping on the MgO surface has been found through the analysis of XRD and the DR-UV/vis spectroscopic data. Furthermore, the obvious shift of MgO peaks to the higher angles was also observed in our study, which was related to the doping of alkali metal ions [49,50]. Therefore, we supposed Mg can be replaced by Li, Na and K in the modeling process.

3.4.1. Oxygen vacancy formation energy

Firstly, the oxygen vacancy formation energies were calculated, which was the prerequisite step for the evaluation of migration energy barrier of oxygen ion in the lattice. Only with the formation of oxygen vacancy, the subsequent migration of oxygen ions can proceed. The optimized structures of pure MgO with perfect surface and oxygen vacancy on the first layer were shown in Fig. 6(a), where the oxygen ion was removed from the perfect surface of MgO. The calculated surface oxygen vacancy formation energy of MgO was 18.84 eV, indicating that the oxygen vacancy formation on the surface of pure MgO is extremely difficult.

For the calculation of the oxygen vacancy formation energy of LiNaK-MgO, the first step was to determine the positions of LiNaK dopants on the MgO surface, which should have the lowest energy. Based on the different shapes arranged by Li, Na and K atoms and their relative positions as well as the symmetry of the structure, there exist thirty-nine configurations of MgO-LiNaK with different arrangements, which was further reduced to nine configurations considering the periodic model. After calculation, the structure with the lowest energy among the nine configurations was shown in Fig. 6(b). A detailed description of the determination of the positions of the dopants was shown in the supplementary.

Based on the stable configuration of the LiNaK-doped MgO surface, four oxygen vacancy formation sites ①-④ were determined in the consideration of symmetry, as shown in Fig. 6(b). The oxygen vacancy formation energy of LiNaK-doped MgO surface at sites ①-④ was calculated, which were corresponding to 1.03, 0.54, 0.37 and 0.86 eV, respectively, where the oxygen at site ③ presents the smallest oxygen vacancy formation energy. Compared with pure MgO, the oxygen vacancy formation energy of LiNaK-MgO decreased significantly from 18.84 to 0.37 eV, proving the promotion of oxygen vacancy formation brought by LiNaK doping.

3.4.2. Structural stability

According to the calculation results of oxygen vacancy formation energy of MgO and MgO-LiNaK, it was clearly known that the oxygen vacancy was extremely difficult to form on the surface of pure MgO, but it easily formed on the surface of MgO-LiNaK. In this section, the formation energy of LiNaK co-doping on the MgO surface with an oxygen vacancy was calculated. Furthermore, the formation energy of further cation incorporation into the subsurface was calculated, which structure was built to explore the effect of the incorporation of cations into deep MgO lattice on the migration of oxygen ion.

Before the formation energy calculation of the cation doping on the subsurface, the doping positions on the subsurface should be determined first, where Li was used as the example for the determination of the cation incorporation position on the subsurface. Four doping sites on the subsurface around the migration oxygen ions were selected, as shown in Fig. 7(a), where the structure with doping site ② presents the lowest energy, which was determined as the cation subsurface doping position.

The structures of LiNaK-doped MgO surface and further cation doping on the subsurface were shown in Fig. 7(b). After calculation, the formation energy of the LiNaK-doped MgO surface was −11.23 eV, and the formation energy of further cation of Li, Na and K doping on the subsurface were corresponding to −9.70, −8.87 and −6.83 eV, respectively. The formation energies of all doping models are negative,

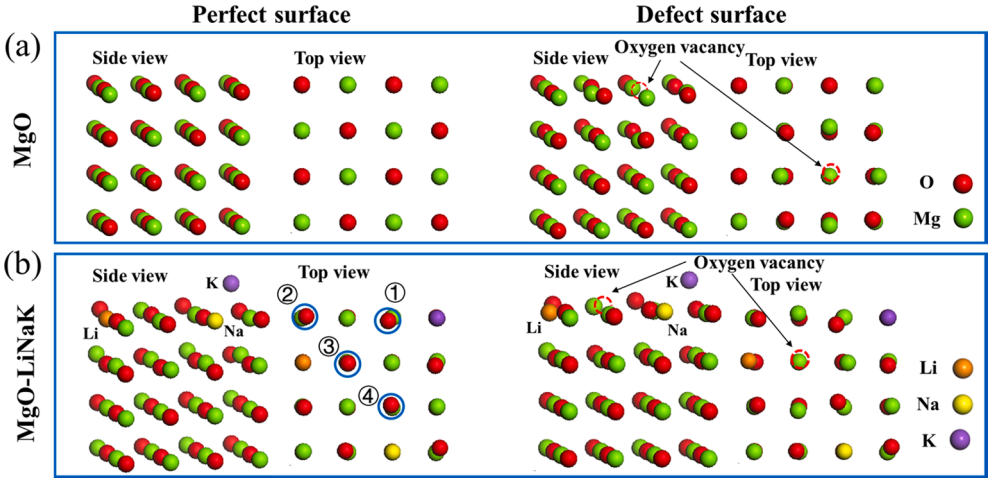

Fig. 6. The optimized structures of (a) MgO and (b) MgO-LiNaK with perfect and defect surfaces.

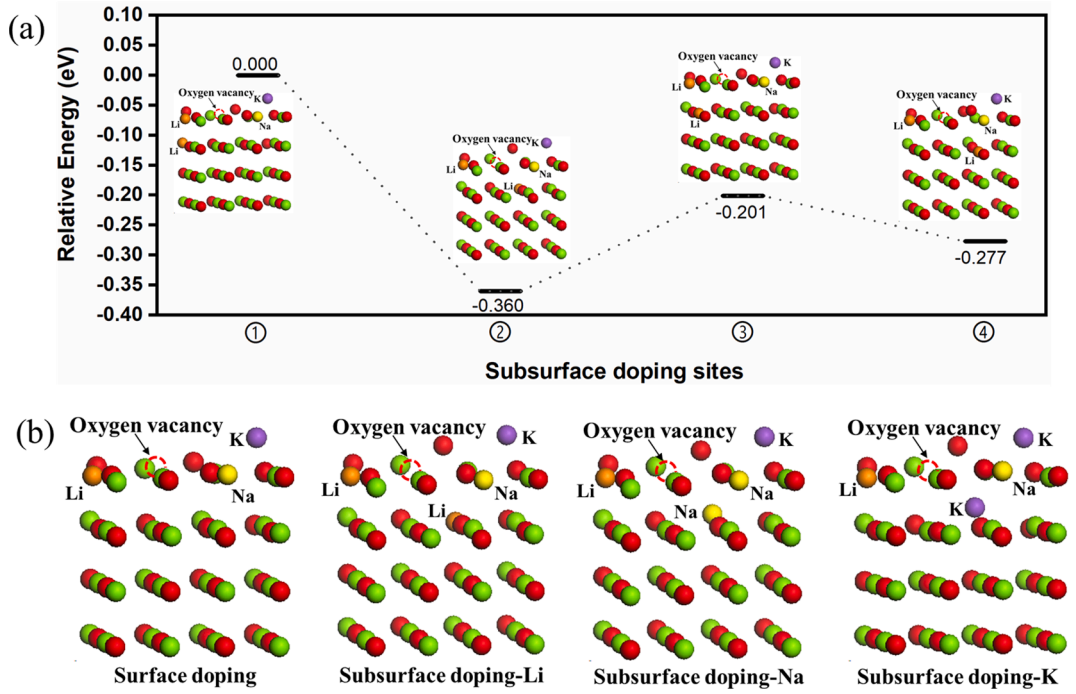

Fig. 7. (a) The relative energy of different Li doping sites on the subsurface and (b) the optimized structures of LiNaK doping surface model and further cation subsurface doping model.

meaning that both LiNaK doping on the surface and further cation doping on the subsurface are stable. The formation energy of the doping on the surface is smaller than that on the subsurface, indicating that surface doping is more stable and the LiNaK surface doping model needs heat absorption for the formation of the further subsurface doping model. Among the further Li, Na and K doping on the subsurface, K doping is the most difficult and Li doping is the easiest.

3.4.3. Migration energy barrier of oxygen ion

The migration energy barrier of oxygen ion in the LiNaK surface doping model and the cation subsurface doping model were calculated and compared. The migration energy barrier of oxygen ion in MgO-LiNaK lattices from the second layer to the first layer is shown in Fig. 8(a), where four different oxygen ion sites on the second layer were selected, which were adjacent to the oxygen vacancy on the top layer. The migration energy barriers of oxygen ion at sites ①-④ were calculated and corresponding to 3.68, 3.83, 3.77 and 4.03 eV, respectively, as shown in Fig. 8(c). The migration energy barrier at site ① possessed the lowest migration energy barrier of 3.68 eV, indicating that the oxygen ion migration path from site ① to the oxygen vacancy is preferred.

For the deep subsurface doping model, the Li subsurface incorporation structure was used as the example to search for the most probable oxygen ion migration path, as shown in Fig. 8(b), where four different oxygen ion sites on the subsurface the same as surface doping model was selected. After calculation, the oxygen ion migration path from site ③ to the oxygen vacancy is preferred with the lowest migration energy barrier of 2.89 eV, as shown in Fig. 8(d). Moreover, the optimized structures of MgO-LiNaK with Na and K doped on the subsurface were built to investigate the effect of different cation subsurface incorporation on the migration of oxygen ion, and the optimized structures at different states during migration were performed as shown in Fig. 8(b). The migration energy barriers of MgO-LiNaK with Na and K incorporation on the subsurface were corresponding to 2.78 and 2.04 eV, respectively, as shown in Fig. 8(e).

The results show that the oxygen ion migration energy of the subsurface doping model was lower than that of the pure MgO (3.68 eV), indicating that deep incorporation of cations promotes the migration of oxygen ion. Among various subsurface doping models, the deep K incorporation presented the minimum value (2.04 eV) compared with Li (2.89 eV) and Na (2.78 eV), revealing that the K incorporation is most effective to promote the migration of oxygen ion. Although the K subsurface doping is the most effective, it was the least easy to form. It seems that the difficulty of the structure formation and the oxygen ion migration correlate with the radius of the deep doping cations, and the larger the radius is, the more energy it needs to form but the easier the oxygen ion migrates.

Based on the above analysis, it can be concluded that the LiNaK doping can effectively reduce the oxygen vacancy formation, and the further deep incorporation of cation lowers oxygen ion migration energy barriers, thus enhancing the oxygen ion diffusion rate in the lattice, which explains the experimental results, where the MgO conversion increased significantly with the initial several cycles. The speculated sorption enhancement mechanism of ETC-promoted MgO sorbent was illustrated in Fig. 9. At the beginning, the ETC was uniformly covered on the surface of MgO as observed from the EDS elemental maps. After the first reaction with CO_2, the LiNaK penetrated downward along with the formation of the product layer of $MgCO_3$. After the regeneration process, oxygen vacancies were formed. With the repeated carbonation and decarbonation process, it absorbed more heat, and more cations penetrate into the depth of MgO with more oxygen vacancies formed, which improved the activity of the MgO, leading to an increased MgO conversion during the cyclic test.

4. Conclusion

In this work, the eutectic carbonates including ETC, Li_2CO_3-Na_2CO_3 and Li_2CO_3-K_2CO_3 were selected as additives for MgO for the CO_2 sorption process conducted at the elevated temperature and pressure due to its higher melting point compared to molten nitrates. MgO-ETC exhibited the highest MgO conversion of 0.93 after 10 cycles with sorption at 515 °C, 5 MPa compared to MgO-(Li_2CO_3-K_2CO_3) and MgO-(Li_2CO_3-Na_2CO_3), whose MgO conversion were corresponding to 0.76 and 0.42, respectively. According to the XRD analysis, the high MgO conversion of MgO-ETC may be attributed to the crystal defects caused

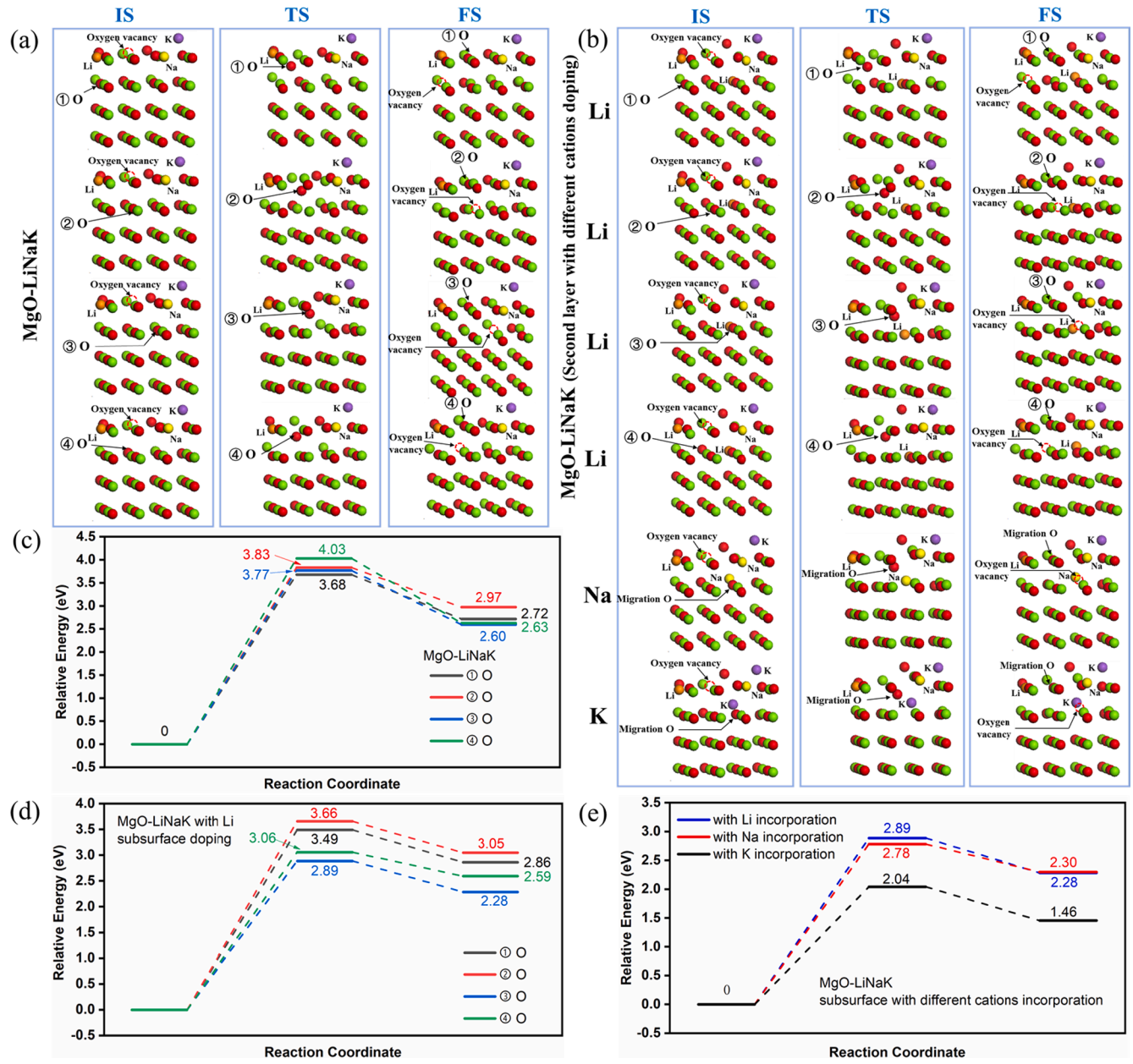

Fig. 8. (a) and (b) The optimized structures of MgO-LiNaK and MgO-LiNaK with different cations doping on the subsurface at different states during migration, (c), (d) and (e) the energy barriers of migration of MgO-LiNaK with different migration path, further Li subsurface doping with different migration path and different cation doping on the subsurface. The IS, TS and FS represent initial, transition and final states.

by the cation incorporation.

Furthermore, the effects of ETC addition amounts and sorption conditions on the MgO conversion were studied during repeated sorption/desorption tests. The synthetic sorbent with the addition of 33 wt% ETC possessed the highest MgO conversion of 0.92 after 30 cycles, and the sorbent with the addition of 20 wt%ETC showed the highest CO_2 capture capacity of 731 mg/g with sorption at 400 °C, 2 MPa. When the test condition was elevated from mild condition (400 °C, 2 MPa) to severe sorption condition (510 °C, 3 MPa), the sorbent could maintain a capture capacity of 786 mg/g after 30 cycles. The sorbent after the cyclic test exhibited a porous structure that decreased the diffusion resistance of CO_2, leading to an excellent cyclic stability under severe sorption conditions. The results indicate that the MgO-ETC sorbent is feasible for the practical application under severe conditions.

In addition, the effects of LiNaK doping on the oxygen vacancy formation and the oxygen ion migration were investigated through the DFT method. The calculation results indicate that the surface oxygen vacancy formation energy decreased dramatically from 18.84 to 0.37 eV with LiNaK doping in comparison with pure MgO, which creates possibilities for oxygen ion migration. Besides, the formation energy and oxygen ion migration energy barrier of LiNaK surface doping and deep cation subsurface doing models were calculated, where the deep K subsurface doping was the most effective strategy to promote the oxygen ion with decreased migration energy barrier from 3.68 to 2.04 eV although it was the most difficult to form. The decreased migration energy barrier reveals that deep incorporation of cations enhanced the oxygen ion diffusion rate from the inner to the surface, which explains the experimental results that the MgO conversion increased significantly with the cycling number in the initial several cycles.

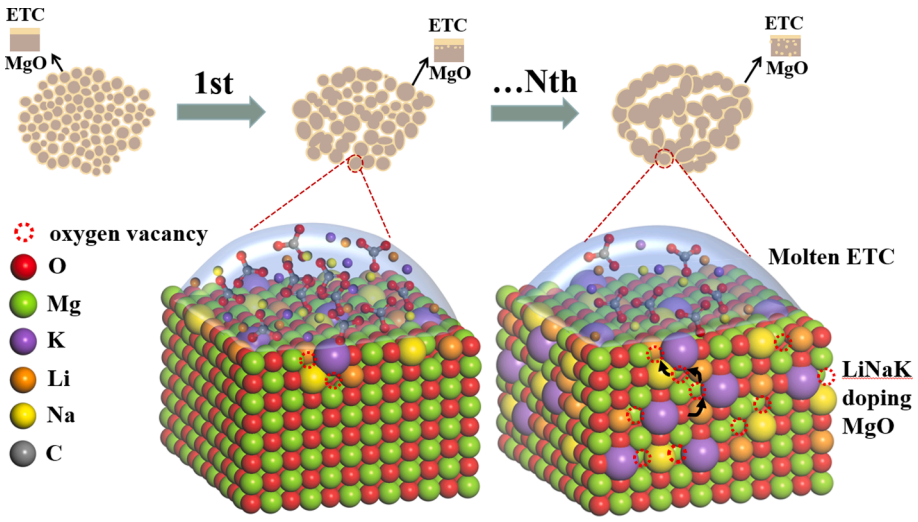

Fig. 9. Illustration of the sorption enhancement mechanism of ETC-promoted MgO sorbent.

CRediT authorship contribution statement

Hua Pang: Methodology, Software, Validation, Formal analysis, Investigation, Writing – original draft. **Feng Mao:** Methodology, Software, Validation, Formal analysis, Writing – review & editing. **Shishun Zhang:** Data curation, Writing – review & editing, Visualization. **Peng Sun:** Writing – review & editing, Visualization. **Anwei Sun:** Writing – review & editing, Visualization. **Gang Xiao:** Conceptualization, Methodology, Resources, Data curation, Writing – review & editing.

Declaration of Competing Interest

The authors declare that they have no known competing financial interests or personal relationships that could have appeared to influence the work reported in this paper.

Data availability

Data will be made available on request.

Acknowledgements

The authors gratefully acknowledge the support from the Zhejiang Provincial Natural Science Foundation (NO.LR20E060001), the Fundamental Research Funds for the Central Universities (2022ZFJH004).

Appendix A. Supplementary data

Supplementary data to this article can be found online at https://doi.org/10.1016/j.apsusc.2023.157207.

References

[1] S.G. Subraveti, K.N. Pai, A.K. Rajagopalan, N.S. Wilkins, A. Rajendran, A. Jayaraman, G. Alptekin, Cycle design and optimization of pressure swing adsorption cycles for pre-combustion CO_2 capture, Appl. Energy 254 (2019) 113624, https://doi.org/10.1016/j.apenergy.2019.113624.

[2] T. Zhang, M. Li, P. Ning, Q. Jia, Q. Wang, J. Wang, K_2CO_3 promoted novel Li_4SiO_4-based sorbents from sepiolite with high CO_2 capture capacity under different CO_2 partial pressures, Chem. Eng. J. 380 (2020) 122515, https://doi.org/10.1016/j.cej.2019.122515.

[3] A. Ys, A. Cs, A. Ql, L.A. Wei, B. Dww, A.J.E.S.M. Az, Tailoring magnesium based materials for hydrogen storage through synthesis: Current state of the art - ScienceDirect, Energy Storage Mater. 10 (2018) 168–198, https://doi.org/10.1016/j.ensm.2017.01.010.

[4] X. Tan, H.A. Tahini, S.C. Smith, Computational design of two-dimensional nanomaterials for charge modulated CO_2 /H_2 capture and/or storage, Energy Storage Mater. 8 (2017) 169–183, https://doi.org/10.1016/j.ensm.2016.12.002.

[5] E.I. Koytsoumpa, C. Bergins, E. Kakaras, The CO_2 economy: Review of CO_2 capture and reuse technologies, J. Supercrit. Fluids 132 (2018) 3–16, https://doi.org/10.1016/j.supflu.2017.07.029.

[6] W.L. Theo, J.S. Lim, H. Hashim, A.A. Mustaffa, W.S.J.A.E. Ho, Review of pre-combustion capture and ionic liquid in carbon capture and storage, Appl. Energy 183 (2016) 1633–1663, https://doi.org/10.1016/j.apenergy.2016.09.103.

[7] X. Zhu, Y. Shi, N. Cai, Integrated gasification combined cycle with carbon dioxide capture by elevated temperature pressure swing adsorption, Appl. Energy 176 (2016) 196–208, https://doi.org/10.1016/j.apenergy.2016.05.068.

[8] S. Jin, K.J. Ko, Y.G. Song, K. Lee, C.H. Lee, Fabrication and kinetic study of spherical MgO agglomerates via water-in-oil method for pre-combustion CO_2 capture, Chem. Eng. J. 359 (2019) 285–297.

[9] A. Hassanzadeh, J. Abbasian, Regenerable MgO-based sorbents for high-temperature CO2 removal from syngas: 1. Sorbent development, evaluation, and reaction modeling, Fuel 89 (6) (2010) 1287–1297, https://doi.org/10.1016/j.fuel.2009.11.017.

[10] S. Zarghami, A. Hassanzadeh, H. Arastoopour, J. Abbasian, Effect of Steam on the Reactivity of MgO-Based Sorbents in Precombustion CO_2 Capture Processes, Ind. Eng. Chem. Res. 54 (36) (2015) 8860–8866, https://doi.org/10.1021/acs.iecr.5b01175.

[11] J. Chi, L. Zhao, B. Wang, Z. Li, Y. Xiao, Y. Duan, Thermodynamic performance assessment and comparison of IGCC with solid cycling process for CO_2 capture at high and medium temperatures, Int. J. Hydrog. Energy 39 (12) (2014) 6479–6491, https://doi.org/10.1016/j.ijhydene.2014.02.005.

[12] S. Jin, K.J. Ko, C.H. Lee, Direct formation of hierarchically porous MgO-based sorbent bead for enhanced CO_2 capture at intermediate temperatures, Chem. Eng. J. 371 (2019) 64–77, https://doi.org/10.1016/j.cej.2019.04.020.

[13] T. Harada, T.A. Hatton, Colloidal Nanoclusters of MgO Coated with Alkali Metal Nitrates/Nitrites for Rapid, High Capacity CO_2 Capture at Moderate Temperature, Chem. Mater. 27 (23) (2015) 8153–8161, https://doi.org/10.1021/acs.chemmater.5b03904.

[14] T. Harada, F. Simeon, E.Z. Hamad, T.A. Hatton, Alkali Metal Nitrate-Promoted High-Capacity MgO Adsorbents for Regenerable CO_2 Capture at Moderate Temperatures, Chem. Mater. 27 (6) (2015) 1943–1949, https://doi.org/10.1021/cm503295g.

[15] Y. Qiao, J. Wang, Y. Zhang, W. Gao, T. Harada, L. Huang, T.A. Hatton, Q. Wang, Alkali Nitrates Molten Salt Modified Commercial MgO for Intermediate-Temperature CO_2 Capture: Optimization of the Li/Na/K Ratio, Ind. Eng. Chem. Res. 56 (6) (2017) 1509–1517, https://doi.org/10.1021/acs.iecr.6b04793.

[16] X. Zhao, G. Ji, W. Liu, X. He, E.J. Anthony, M. Zhao, Mesoporous MgO promoted with $NaNO_3$/$NaNO_2$ for rapid and high-capacity CO_2 capture at moderate temperatures, Chem. Eng. J. 332 (2017) 216–226, https://doi.org/10.1016/j.cej.2017.09.068.

[17] M.L.T. Trivino, H. Jeon, A.C.S. Lim, V. Hiremath, Y. Sekine, J.G. Seo, Encapsulation of Phase-Changing Eutectic Salts in Magnesium Oxide Fibers for High-Temperature Carbon Dioxide Capture: Beyond the Capacity-Stability Tradeoff, ACS Appl. Mater. Interfaces 12 (1) (2020) 518–526, https://doi.org/10.1021/acsami.9b15632.

[18] V. Hiremath, M.L.T. Trivino, J.G. Seo, Eutectic mixture promoted CO2 sorption on MgO-TiO2 composite at elevated temperature, J Environ Sci (China) 76 (2019) 80–88, https://doi.org/10.1016/j.jes.2018.03.028.

[19] S. Jin, K. Ho, C.H. Lee, Facile synthesis of hierarchically porous MgO sorbent doped with $CaCO_3$ for fast CO_2 capture in rapid intermediate temperature swing sorption, Chem. Eng. J. 334 (2018) 1605–1613, https://doi.org/10.1016/j.cej.2017.11.095.

[20] H. Cui, Q. Zhang, Y. Hu, C. Peng, X. Fang, Z. Cheng, V.V. Galvita, Z. Zhou, Ultrafast and Stable CO_2 Capture Using Alkali Metal Salt-Promoted MgO-$CaCO_3$ Sorbents, ACS Appl. Mater. Interfaces 10 (24) (2018) 20611–20620, https://doi.org/10.1021/acsami.8b05829.

[21] H. Cui, Z. Cheng, Z. Zhou, Unravelling the role of alkaline earth metal carbonates in intermediate temperature CO_2 capture using alkali metal salt-promoted MgO-based sorbents, J. Mater. Chem. A 8 (35) (2020) 18280–18291, https://doi.org/10.1039/d0ta06170k.
[22] H. Pang, H. Xu, A. Sun, G. Xiao, Characteristics of MgO-based sorbents for CO_2 capture at elevated temperature and pressure, Appl. Surf. Sci. 598 (2022) 153852, https://doi.org/10.1016/j.apsusc.2022.153852.
[23] K. Zhang, X.S. Li, H. Chen, P. Singh, D.L. King, Molten Salt Promoting Effect in Double Salt CO_2 Absorbents, J. Phys. Chem. C 120 (2) (2015) 1089–1096, https://doi.org/10.1021/acs.jpcc.5b10729.
[24] A. Dal Pozzo, A. Armutlulu, M. Rekhtina, P.M. Abdala, C.R. Müller, CO_2 Uptake and Cyclic Stability of MgO-Based CO_2 Sorbents Promoted with Alkali Metal Nitrates and Their Eutectic Mixtures, ACS Appl. Energy Mater. 2 (2) (2019) 1295–1307, https://doi.org/10.1021/acsaem.8b01852.
[25] H. Lee, M.L.T. Trivino, S. Hwang, S.H. Kwon, S.G. Lee, J.H. Moon, J. Yoo, J.G. Seo, In Situ Observation of Carbon Dioxide Capture on Pseudo-Liquid Eutectic Mixture-Promoted Magnesium Oxide, ACS Appl. Mater. Interfaces 10 (3) (2017) 2414–2422, https://doi.org/10.1021/acsami.7b14256.
[26] S. Jin, K. Ho, A.T. Vu, C.H. Lee, Salt-Composition-Controlled Precipitation of Triple-Salt-Promoted MgO with Enhanced CO_2 Sorption Rate and Working Capacity, Energy Fuels 31 (9) (2017) 9725–9735, https://doi.org/10.1021/acs.energyfuels.7b01428.
[27] R.M. German, P. Suri, S.J. Park, Liquid phase sintering, J. Mater. Sci. 44 (1) (2009) 1–39, https://doi.org/10.1007/s10853-008-3008-0.
[28] M.G. Gardeh, A.A. Kistanov, H. Nguyen, H. Manzano, W. Cao, P. Kinnunen, Exploring Mechanisms of Hydration and Carbonation of MgO and $Mg(OH)_2$ in Reactive Magnesium Oxide-Based Cements, J. Phys. Chem. C Nanomater. Interfaces 126 (14) (2022) 6196–6206, https://doi.org/10.1021/acs.jpcc.1c10590.
[29] M.M. Kenisarin, High-temperature phase change materials for thermal energy storage, Renew. Sustain. Energy Rev. 14 (3) (2010) 955–970, https://doi.org/10.1016/j.rser.2009.11.011.
[30] J. Luo, C.K. Deng, N.u.H. Tariq, N. Li, R.F. Han, H.H. Liu, J.Q. Wang, X.Y. Cui, T. Y. Xiong, Corrosion behavior of SS316L in ternary Li_2CO_3–Na_2CO_3–K_2CO_3 eutectic mixture salt for concentrated solar power plants, Sol. Energy Mater. Sol. Cells 217 (2020) 110679.
[31] F. Yuan, M.J. Li, Z. Ma, Bo. Jin, Z.B. Liu, Experimental study on thermal performance of high-temperature molten salt cascaded latent heat thermal energy storage system, Int. J. Heat Mass Transf. 118 (2018) 997–1011, https://doi.org/10.1016/j.ijheatmasstransfer.2017.11.024.
[32] S. Li, F. Bruno, Y. Sun, Y. Jiang, Thermal stability of Na_2CO_3-Li_2CO_3 as a high temperature phase change material for thermal energy storage, Thermochim Acta 650 (2017) 88–94, https://doi.org/10.1016/j.tca.2017.01.002.
[33] K. Li, N.i. Li, N. Yan, T. Wang, Y. Zhang, Q. Song, H. Li, Adsorption of small hydrocarbons on pristine, N-doped and vacancy graphene by DFT study, Appl. Surf. Sci. 515 (2020) 146028.
[34] C.P. Zhang, B. Li, Z.G. Shao, First-principle investigation of CO and CO_2 adsorption on Fe-doped penta-graphene, Appl. Surf. Sci. 469 (2019) 641–646, https://doi.org/10.1016/j.apsusc.2018.11.072.
[35] H. Zhao, N. Qi, Y. Li, Interaction between polysaccharide monomer and SiO_2/Al_2O_3/$CaCO_3$ surfaces: A DFT theoretical study, Appl. Surf. Sci. 466 (2019) 607–614, https://doi.org/10.1016/j.apsusc.2018.10.085.
[36] F. Ortmann, F. Bechstedt, W.G. Schmidt, Semiempirical van der Waals correction to the density functional description of solids and molecular structures, Phys. Rev. B 73 (20) (2006), https://doi.org/10.1103/PhysRevB.73.205101.
[37] S. Grimme, Semiempirical GGA-type density functional constructed with a long-range dispersion correction, J. Comput. Chem. 27 (15) (2010) 1787–1799, https://doi.org/10.1002/jcc.20495.
[38] A. Parameswari, Y. Soujanya, G.N. Sastry, Functionalized Rutile TiO_2(110) as a Sorbent To Capture CO_2 through Noncovalent Interactions: A Computational Investigation, J. Phys. Chem. C 123 (6) (2019) 3491–3504, https://doi.org/10.1021/acs.jpcc.8b09311.
[39] S. Kwon, J.I. Choi, S.G. Lee, S.S. Jang, A density functional theory (DFT) study of CO_2 adsorption on Mg-rich minerals by enhanced charge distribution, Comput. Mater. Sci 95 (2014) 181–186, https://doi.org/10.1016/j.commatsci.2014.07.042.
[40] N.H. de Leeuw, G.W. Watson, S.C. Parker, Atomistic Simulation of the Effect of Dissociative Adsorption of Water on the Surface Structure and Stability of Calcium and Magnesium Oxide, J. Phys. Chem. 99 (47) (1995) 17219–17225.
[41] A.M. Ritzmann, A.B. Muñoz-García, M. Pavone, J.A. Keith, E.A. Carter, Ab Initio DFT+U Analysis of Oxygen Vacancy Formation and Migration in La 1-x Sr x FeO 3-δ (x = 0, 0.25, 0.50), Chem. Mater. 25 (15) (2013) 3011–3019.
[42] X. Ma, Y. Li, W. Zhang, Z. Wang, J. Zhao, DFT study of CO_2 adsorption across a CaO/$Ca_{12}Al_{14}O_{33}$ sorbent in the presence of H_2O under calcium looping conditions, Chem. Eng. J. 370 (2019) 10–18, https://doi.org/10.1016/j.cej.2019.03.176.
[43] T. Zhang, H. Yin, C. Zhang, R. Zhang, X. Jiang, Q. Zheng, X. Qu, First-Principles Study on the Mechanical Properties and Electronic Structure of V Doped WCoB and W_2CoB_2 Ternary Borides, Materials (Basel) 12 (6) (2019), https://doi.org/10.3390/ma12060967.
[44] L. Lin, Z. Shi, J. Huang, P. Wang, W. Yu, C. He, Z. Zhang, Molecular adsorption properties of CH_4 with noble metals doped onto oxygen vacancy defect of anatase TiO_2 (1 0 1) surface: First-principles calculations, Appl. Surf. Sci. 514 (2020) 145900.
[45] Y. Lee, S. Lee, Y. Hwang, Y.-C. Chung, Modulating magnetic characteristics of Pt embedded graphene by gas adsorption (N_2, O_2, NO_2, SO_2), Appl. Surf. Sci. 289 (2014) 445–449, https://doi.org/10.1016/j.apsusc.2013.10.189.
[46] S. Dillinger, J. Lang, G. Niedner-Schatteburg, Cryo IR Spectroscopy of [Hemin](+) Complexes in Isolation, J Phys Chem A 121 (38) (2017) 7191–7196, https://doi.org/10.1021/acs.jpca.7b08604.
[47] Y. Ortega, O. Lamiel-Garcia, D.F. Hevia, S. Tosoni, J. Oviedo, M.A. San-Miguel, F. Illas, Theoretical study of the Fluorine doped anatase surfaces, Surf. Sci. 618 (2013) 154–158, https://doi.org/10.1016/j.susc.2013.09.010.
[49] J.S. Kwak, K.Y. Kim, J.W. Yoon, K.R. Oh, Y.U. Kwon, Interfacial Interactions Govern the Mechanisms of CO_2 Absorption and Desorption on A_2CO_3-Promoted MgO (A = Na, K, Rb, and Cs) Absorbents, J. Phys. Chem. C. Nanomater. Interfaces 122 (35) (2018) 20289–20300, https://doi.org/10.1021/acs.jpcc.8b04895.
[50] U. Zavyalova, G. Weinberg, W. Frandsen, F. Girgsdies, T. Risse, K.P. Dinse, R. Schloegl, R. Horn, Lithium as a Modifier for Morphology and Defect Structure of Porous Magnesium Oxide Materials Prepared by Gel Combustion Synthesis, ChemCatChem 3 (11) (2011) 1779–1788, https://doi.org/10.1002/cctc.201100146.